energies

MDPI

Article

Computationally Efficient Modeling of DC-DC Converters for PV Applications

Fabio Corti [1], Antonino Laudani [2], Gabriele Maria Lozito [2,*] and Alberto Reatti [1]

[1] Department of Information Engineering, University of Florence, Via di S.Marta 3, 50139 Florence, Italy; fabio.corti@unifi.it (F.C.); alberto.reatti@unifi.it (A.R.)
[2] Engineering Department, Roma Tre University, Via Vito Volterra 62b, 00146 Roma, Italy; alaudani@uniroma3.it
* Correspondence: gabrielemaria.lozito@uniroma3.it

Received: 26 August 2020; Accepted: 28 September 2020; Published: 30 September 2020

Abstract: In this work, a computationally efficient approach for the simulation of a DC-DC converter connected to a photovoltaic device is proposed. The methodology is based on a combination of a highly efficient formulation of the one-diode model for photovoltaic (PV) devices and a state-space formulation of the converter as well as an accurate steady-state detection methodology. The approach was experimentally validated to assess its accuracy. The model is accurate both in its dynamic response (tested in full linearity and with a simulated PV device as the input) and in its steady-state response (tested with an outdoor experimental measurement setup). The model detects automatically the reaching of a steady state, thus resulting in lowered computational costs. The approach is presented as a mathematical model that can be efficiently included in a large simulation system or statistical analysis.

Keywords: DC-DC converters; photovoltaics; single-diode model; state-space

1. Introduction

Modeling the dynamic behavior of a photovoltaic power system is a challenging and actual topic due to its nonlinear nature and its dependence on environmental quantities [1]. The whole conversion system is, in general, composed of several photovoltaic devices, DC-DC conversion stages, energy storage units, and, usually, an inverter for grid connection. Considering the chain from the end, grid-connected inverters are usually well-understood, and considerable literature can be found on modeling both their AC and transient responses [2–4]. Most researches consider parasitic components that highly affect the converter operation, using both a linear equivalent circuit approach and state-space averaging methods [5–13]. On the other hand, energy storage is an open topic considering the wide options for storage technologies that are available or rising [14,15]. The DC stage is considerably simple to model when the input voltage can be considered an ideal source; however, a nonlinear device such as a photovoltaic (PV) panel can void several assumptions used for the simple steady-state modeling of the DC converter. Electrical modeling of a PV device involves an interaction with the environmental variables of irradiance (G) and temperature (T) to correctly represent the voltage-current relationship of the device. The assessment and forecasting of such quantities, especially irradiance, is an open problem in the literature [16–19]. Modeling the PV device connected to a DC converter can be difficult, computationally intensive, and might lead to numerical instability. A complete overview of the issues related can be found in [1,4,20], where the stability of the control process is discussed in an exhaustive way, including the problematics related to maximum power point tracking and small-signal modeling of the PV source. The reading of [4,20] is also important to better understand the differences raised when the PV source is considered equivalent to a voltage or current source. The purpose of this work

is to address the difficulties in modeling the nonlinearity of the PV source characteristic by discussing a computationally efficient implementation of the model. Two key aspects are optimized. The first one involves the simulation of the PV device by means of the single-diode model (in the version of a five-parameters model) [21,22]. This circuit model is accurate on the majority of silicon devices, under variable environmental conditions [23]. This individual element of the framework was chosen with solid foundations in state-of-the-art approaches. The single-diode model is a preferred choice for the vast majority of PV literature, both for its computational speed and the wide options for model identification algorithms available. The model was implemented in the framework, with some recent optimizations to enhance the numerical stability. Through the application of the Lambert W function, two explicit relationships can be formulated [24]: the voltage can be written as a function of the current or the current can be written as a function of the voltage, i.e., the PV source becomes equivalent to a current-controlled voltage source (CCVS) or to a voltage-controlled current source (VCCS). However, for some operating conditions of the one-diode model, an exponential overflow can cause divergence in the Lambert function expressions. This shortcoming is addressed through an additional functional mapping [25,26]. The second optimization involves the transient simulation of the DC-DC converter connected to the PV device. A procedure to predict the steady-state value of the state variables is proposed. Using this knowledge, the transient simulation can be halted as soon as a steady state is reached. It should be underlined that this work aims to create an efficient framework for the simulation of a DC-DC converter in the presence of a PV input; thus, the steady-state detection approach is its core concept, since it is able to shorten drastically the computational times. This is particularly important since a time domain analysis is performed to remark the nonlinear and time-varying behaviors of the PV source.

The accuracy of the proposed modeling approach was validated experimentally on three workbenches. The first one to assess the dynamic model of the DC-DC converter without the nonlinearity introduced by the PV device. The second to assess the accuracy of the steady-state predicting procedure when a real PV device is connected to the DC-DC converter. The third one to assess the accuracy of the transient response for the full DC-DC converter plus PV device system, making use of a PV device electrical emulator and a programmable DC load.

An important contribution comes from the presentation of the proposed approach. The majority of the simulations involving DC-DC converters and PV devices found in the literature make use of circuit simulation software [27–29]. The further inclusion of these simulations in larger analyses (e.g., Monte Carlo or a grid simulation for machine-learning purposes [30–32]) is difficult and unpractical. The approach proposed in this work, on the other hand, is presented in the form of clear mathematical models that can be implemented in any programming language.

The paper is structured as follows. In Section 2, the proposed model is described as composed by the PV device model, the transient and steady-state model for the DC-DC converter, and the steady-state prediction procedure, along with a computational costs discussion. In Section 3, the sizing and hardware implementation of the DC-DC converter is described. The three experimental validation workbenches are described, and the results are presented in Section 4. Final considerations and conclusions close the manuscript.

2. The Proposed Model

The model presented in this work represents a photovoltaic device connected to a DC-DC converter with a resistive load. The nature of the real system to represent includes both the electrical behavior of the DC-DC converter and the nonlinear, environmental-dependent nature of the PV device. The model aims to represent the electrical behavior of the full system with a good accuracy, with reduced computational costs both in the transient and steady state operations. This is achieved through a lean reformulation of the current-voltage relationship for a single-diode model, a state-space formulation for the DC-DC converter, and, most importantly, an effective strategy for steady-state detection.

2.1. Single-Diode Model for Transient Simulations

The single-diode model is an equivalent circuit model that can be used to represent the electrical behavior of a PV device with arbitrary conditions of irradiance (G) and temperature (T). The circuital representation of the model is shown in Figure 1 It should be noted that the single-diode model is meant to represent a single PV cell. However, under the assumptions of uniform irradiance and temperature, it can be used to represent an arbitrary series and parallel of PV cells. Thus, it is suitable to represent PV panels, strings, and arrays.

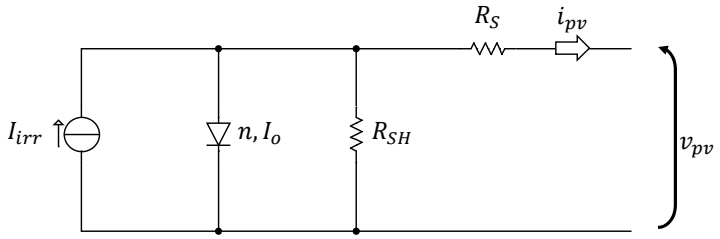

Figure 1. Single-diode equivalent circuit model for a photovoltaic (PV) device.

Considering the only part of the circuit where the voltage (v_{pv}) and current (i_{pv}) are defined in an active sign convention, the voltage-current relationship of this model can be easily derived by applying the Kirchhoff Current Law. As can be seen, it is nonlinear, transcendent, and implicit.

$$I_{irr} - I_o\left[\exp\left(\frac{v_{pv} + R_S\, I_{pv}}{n\ V_t}\right) - 1\right] - \frac{v_{pv} + R_S\, i_{pv}}{R_{SH}} - i_{pv} = 0 \tag{1}$$

The five parameters of the model are plainly apparent in the equation, where I_{irr} is the generated photocurrent, I_o is the diode reverse saturation current, n is the ideality factor, R_S is the series resistance, and R_{SH} is the shunt resistance. Since (1) describes the voltage-current relationship of the device, the general application involves the determination of the current for a known device voltage or vice-versa. Unfortunately, since (1) is implicit and transcendent, the only way to solve it is by using iterative root-finding techniques, such as the Newton-Raphson method, fixing either the voltage or the current, and solving the equation for the missing variable. This approach is very common and is acceptably fast but, as will be shown below, lacks a proper explicit formulation.

Regardless of the difficulty in solving (1), the single-diode model must be identified prior to being able to represent a physical device. Identification of the model (over a physical device) consists in the determination of the five parameters that results in the best fit with the electrical characteristic of the device at the standard reference conditions, SRC (T = 25 °C and G = 1000 W/m^2). Several methodologies exist in the literature that allow identification either from experimental measurements [25,33] or quantities from the constructor datasheet [22].

Since the circuit model of the device is identified at the SRC, the model must be completed by a set of equations [23] that express a dependence of the five circuit parameters from the environmental conditions of irradiance (G) and temperature (T).

$$R_S = R_{S,ref} \tag{2}$$

$$n = n_{ref} \tag{3}$$

$$R_{sh} = R_{sh,ref}\left(\frac{G}{G_{ref}}\right) \tag{4}$$

$$I_{irr} = I_{irr,ref}\left(\frac{G_{ref}}{G}\right)\left[1 + \alpha\left(T - T_{ref}\right)\right] \tag{5}$$

$$I_0 = I_{0,ref}\left(\frac{T}{T_{ref}}\right)^3 \exp\left[\frac{E_g\left(T_{ref}\right)}{kT_{ref}} - \frac{E_g(T)}{kT}\right] \tag{6}$$

Through this set of equations, it is possible to update the electrical characteristic of the model for a time-variable profile of irradiance and temperature, which is the classic scenario for a real PV device. The subscript *ref* is for the parameters when the model represents the device at the SRC. The other symbols are k for the Boltzmann constant, α for the temperature coefficient for the open-circuit current, and E_g (T) is the temperature-dependent bandgap energy of the semiconductor used for the device construction. If this current-voltage (I-V) relationship is to be included in a transient analysis, such as the one for a DC-DC converter, for each time step, a nonlinear root-finding problem should be solved, with an added computational burden. This is especially true if several PV devices are connected in a series or in parallel. A first reformulation of this relationship is found in the literature through the means of the Lambert W function, resulting in two expressions [24]:

$$v_{pv}\left(i_{pv}\right) = R_{SH}(I_{irr} + I_o) - (R_S + R_{SH})i_{pv} - nV_t\,\mathrm{W}\left[\frac{I_o R_{SH}}{nV_t}\exp\frac{R_{SH}\left(I_{irr} + I_o - i_{pv}\right)}{nV_t}\right] \tag{7}$$

$$i_{pv}\left(v_{pv}\right) = -\frac{nVt}{R_S}\mathrm{W}\left[\frac{R_S}{nV_t} * \frac{I_0 R_{SH}}{R_{SH} + R_S} * \exp\left(\frac{R_{SH}}{R_S + R_{SH}}\frac{v_{pv} + R_S(I_{irr} + I_o)}{nV_t}\right)\right] + \frac{(I_{irr} + I_o)R_{SH} - v_{pv}}{R_{SH} + R_S} \tag{8}$$

This reformulation moves the computational burden of the root-finding algorithm from the solution of a generic equation to the solution of the Lambert W function for a positive argument. Although the explicit current relationship (8) is, in general, without computational problems, the same cannot be said for the explicit voltage relationship [25,26]. When very large arguments appear in the exponential used in (7), which is limited to arguments below ~700 in a 64-bit double-precision float computation environment, the overflow may lead to divergence. A possible solution involves using a mapping function such as the one in (9) and (10).

$$\mathrm{g}(z) = \ln[W \cdot \exp(z)] \tag{9}$$

$$\mathrm{g}(z) + \exp[g(z)] = z \tag{10}$$

From this mapping, the explicit voltage relationship is

$$v_{pv}\left(i_{pv}\right) = -i_{pv} \cdot R_S + n \cdot V_t\left[g(z) - \ln\left(\frac{I_o R_{SH}}{nV_t}\right)\right] z = \ln\left(\frac{I_o R_{SH}}{nV_t}\right) + \frac{R_{SH}\left(I_{irr} + I_o - i_{pv}\right)}{nV_t} \tag{11}$$

which can be used along with (8) to include the I-V relationship of a PV device in any Kirchhoff circuital equation resulting from a state-space analysis of a dynamic circuit.

2.2. Transient Model for the DC-DC Converter

The topology investigated in this work is a classic buck-boost converter. This topology is useful both for load-oriented applications (e.g., battery charging and equalization [34,35]) and source-oriented applications (e.g., maximum power point tracking [36]). The circuit model, featuring the main parasitic elements, is shown in Figure 2 where, C_{IN} is a capacitor stabilizing the converter input voltage, R_{ds} is the on resistance of the controlled switch (e.g. a power MOSFET), R_L is the inductor L equivalent series resistance, V_{fwd} is the diode threshold voltage, R_D is the diode conduction resistance, C is the converter output capacitance and R is the converter load resistance; moreover, i_{pv} is the panel output current, i_L is the inductor current, v_{CIN} is the voltage across the input capacitor and, v_C is the voltage across the output. Since the purpose of this work is to create a model able to represent the full system both in the transient and steady states, the first step involves the identification of the state variables of the system and the derivation of the relative state equations. The system is commuted through a switch and a

diode, and for this reason, two sets of state equations needs to be defined: one for the ON state and one for the OFF state. Through simple observations, the ON and OFF state equations of the circuit can be derived.

$$ON: \begin{cases} \dot{x}_1 = \frac{1}{C}\left(-\frac{x_1}{R}\right) \\ \dot{x}_2 = \frac{1}{L}[x_3 - (R_{DS} + R_L)x_2] \\ \dot{x}_3 = \frac{1}{C_{IN}}\left[i_{pv}(x_3) - x_2\right] \end{cases} \quad (12)$$

$$OFF: \begin{cases} \dot{x}_1 = \frac{1}{C}\left(-\frac{x_1}{R} - x_2\right) \\ \dot{x}_2 = \frac{1}{L}\left(-x_2 R_L + x_1 - V_{fwd} - R_D x_2\right) \\ \dot{x}_3 = \frac{1}{C_{IN}}\left[i_{pv}(x_3)\right] \end{cases} \quad (13)$$

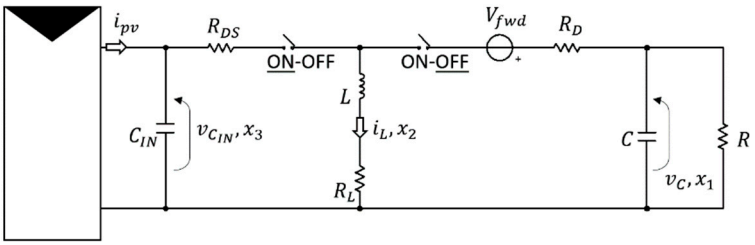

Figure 2. Circuit model for the PV device connected to the DC-DC converter, highlighting the parasitic components.

The state variables appearing in (12) and (13) are the following: x_1 is the voltage across the output capacitor, x_2 is the current through the inductor, and x_3 is the voltage across the input capacitor. As can be seen in the last state equation, the I-V relationship of the PV device affects the current of the input capacitor. This is the only nonlinearity present in the dynamic model of the system. The PV device is connected directly in parallel with the input capacitor, and since its voltage is known at each time step (being a state variable), the most convenient choice to express the PV electrical relationship is (8), and consequently, it acts as the VCCS. However, if a more complex converter was implemented, or if, for some reason, the input capacitor was to be removed, the series connection between the PV device and the main inductor L would result in a more practical choice of (11) as the relationship to represent the PV device.

The state equations can be integrated numerically to create a time response of the system. Assuming a variable profile for irradiance and temperature, the PV circuit parameters (and thus, the resulting state equations) can be updated by means of (2)–(6). As the system reaches a steady state, the integration can halt, and the simulation can proceed with a steady-state linearized model. Since the system is nonlinear, it is impossible to estimate the steady state from the time constants, and it must be manually detected by observing the state variables.

2.3. Steady-State Detection and Modeling

In a steady state, it is safe to assume that the large capacitor in parallel with the PV device has a stable and constant voltage across it. From a system point of view, this transforms the former state variable in a system input. Since the nonlinearity is hidden behind this input, it is possible to approach the DC-DC converter simulation with classic tools such as defining the transfer function via the state-space average (SSA) [37,38]. With reference to the first two equations of (12) and (13), the linearized and averaged system is shown in (14), where V_{IN} is the constant voltage across the C_{IN} input capacitor. This new system can be integrated analytically or numerically with a large time step for reduced computational costs.

$$\overline{A} = \begin{bmatrix} -\frac{1}{RC} & \frac{D-1}{C} \\ \frac{1-D}{L} & \frac{D(R_D - R_{DS}) - (R_L + R_D)}{L} \end{bmatrix}; \overline{B} = \begin{bmatrix} 0 & 0 \\ \frac{D}{L} & \frac{D-1}{L} \end{bmatrix}; u = \begin{bmatrix} V_{IN} \\ V_{fwd} \end{bmatrix}; x = \begin{bmatrix} x_1 \\ x_2 \end{bmatrix} \dot{x} = \overline{A}x + \overline{B}u \quad (14)$$

From the SSA system, by assuming a steady state, three transfer functions can be easily derived:

$$\frac{V_{OUT}}{V_{IN}} = \frac{-D}{(D-1) + \frac{D(R_D - R_{DS}) - (R_L + R_D)}{R(1-D)}} \tag{15}$$

$$\frac{I_{OUT}}{I_{IN}} = \frac{1-D}{D} \tag{16}$$

$$\frac{R_{OUT}}{R_{IN}} = \frac{-D^2}{(1-D)\left[(D-1) + \frac{D(R_D - R_{DS}) - (R_L + R_D)}{R(1-D)}\right]} \tag{17}$$

Indeed, in (17), the R on the right-hand side of the equation is equal to R_{OUT}. The transfer functions can be used as a method to detect the steady state through these simple steps:

- Using (17), find the equivalent input load seen by the PV panel across the DC-DC converter.
- Find the operating point of the PV panel through (11) or (8) and the steady-state input voltage $V_{IN,SS}$.
- Using (15), determine the steady-state output voltage $V_{OUT,SS}$.
- Calculate the output current with Ohm's law, then use (16) to determine the input current $I_{IN,SS}$.
- Calculate the average current through the inductor as $I_{L,SS} = I_{IN,SS}/D$.
- To determine the accuracy of the steady state, compare x_1 with $V_{OUT,SS}$, x_2 with $I_{IN,SS}$, and x_3 with $V_{IN,SS}$.

An example of this comparison is shown in Figure 3 for three different values of duty cycle D (0.4, 0.5, and 0.6). The transient reaches a steady-state value that is very close to the predicted steady-state value obtained through the (15)–(17) transfer functions. From an implementation point of view, since the electric quantities are averagely constant once a steady state is reached, the simulation can be halted or, if needed, can be performed with very large time steps using (14), which can hold for small perturbations as well. This results in an almost negligible computational cost. On the other hand, if a large perturbation (e.g., on the load or in the environmental conditions of the PV device) occurs, it is possible to restart the transient simulation using the steady-state quantities of $V_{OUT,SS}$, $I_{L,SS}$, and $V_{IN,SS}$ as the initial conditions for the three state variables: $x_1, x_2,$ and x_3.

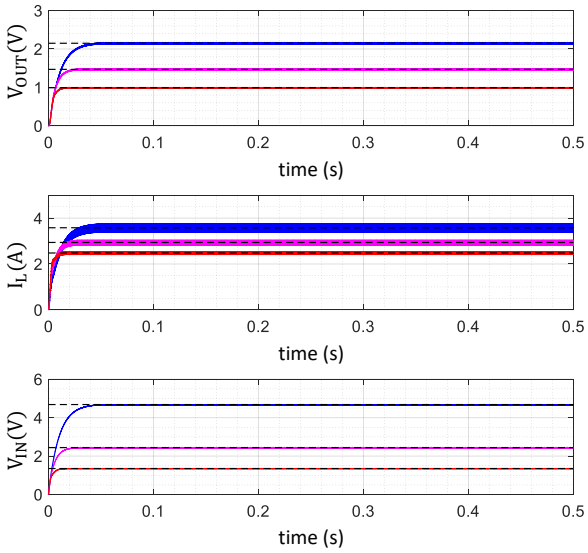

Figure 3. Comparison between the transient solution of the circuit (full-colored lines) and the estimated steady-state value of the three state variables (dashed black lines). The blue curve is relative to $D = 0.4$, magenta to $D = 0.5$, and red to $D = 0.6$.

2.4. Computational Costs

The model computational load is only relevant for the transient part and is composed by the short time-step integration of (12) and (13). Inside this computation, a large contribution to the computational cost comes from the solution of (8) by means of the Lambert W function at each time step. The model was profiled for performance on a Core i7 Windows 10 machine running Matlab2020a by The Mathworks, Inc., Natick, Massachusetts (MA)considering a variable number of time steps (from 6400 to 640,000) to account for the memory usage effects. The average computational time for a single time step is 4.213×10^{-5} s. The contribution from the solution of (8), considering the variable irradiance and temperature (thus, considering the use of (4)–(6) for parameter updates) is 1.731×10^{-5} s. In other words, more than 40% of the computational burden is related to the nonlinear nature of the problem and, in particular, to the solution of the Lambert W function found in (8) (or the g function found in (11), in case a voltage relation is needed).

The costs involved for the transient part of the model are considerable and would lead to long computational times for simulations. In this context, the ability to quickly switch into a simpler steady-state model after the transient is exhausted is a strong feature that makes this approach suitable for further integrations into more complex analysis protocols, such as Monte Carlo optimizations.

3. DC-DC Converter

To validate the proposed model, a DC-DC converter was built to interface the load with the photovoltaic panel. The converter constraints are summarized in Table 1.

Table 1. System parameters.

Parameter	Value	Description
f_0	20 kHz	Switching Frequency
D	0.3–0.6	Duty Cycle Range
$V_{i,max}$	33.3 V	Maximum Input Voltage
I_o	6.67–40 A	Output Current
R_L	0-20 Ω	Load Resistance
ΔV_o	0.3 V	Maximum Output Ripple
P_o	100–295 W	Output Power

The procedure given in [8,39] is used for the DC-DC converter design. The average output current is calculated as

$$I_o = \frac{I_o^{\max} + I_o^{\min}}{2} = 23.34 \text{ A} \tag{18}$$

The inductor average current is expressed as

$$I_L = \frac{I_o}{1 - D} \tag{19}$$

Thus, the inductor average current I_L depends on the duty cycle. If the system operates at $D = D_{\max} = 0.6$, the current is $I_L^{\max} = 58.34$ A, while if the converter operates at $D = D_{\max} = 0.3$, the current is $I_L^{\min} = 33.34$ A.

The minimum value of inductance needed to operate in continuous conduction mode (CCM) is

$$L_{\min} = \frac{R_L^{\max}(1 - D_{\min})^2}{2f} = 184 \text{ μH} \tag{20}$$

while the minimum capacitance needed to operate at the desired output voltage ripple is

$$C_{\min} = \frac{I_0^{\max} D_{\min}}{f\left[\Delta V_o - \left(\frac{I_0^{\max}}{1-D} + \frac{\Delta I_L}{2}\right) ESR_C\right]} = 578\ \mu\text{F} \tag{21}$$

The input capacitance is used to hold up the input voltage during the time when the energy is decreasing in the inductor.

If the input voltage drop should not be bigger than the input voltage ripple ΔV_{in}, the minimum effective value for this capacitor $C_{IN}^{\min}$ is estimated with

$$C_{IN}^{\min} = \frac{I_L D^{\max}}{f\left[\Delta V_{in} - \Delta I_L ESR_{C_{IN}}\right]} = 1.73\ \text{mF} \tag{22}$$

Equation (10) in [40] implies that higher equivalent series resistance of the capacitor (ESR) increases the input voltage drop. A SCT3022AL SiC power Mosfet driven by a 1EDC60H12AH isolated gate driver is used in the Buck-Boost converter.

The Mosfet has a breakdown voltage V_{DSS} = 650 V and a nominal conduction resistance of r_{DS} = 22 mΩ. A FFSP2065B SiC diode with a reverse voltage V_{RRM} = 650 V and a continuous rectified forward current I_F = 20 A is used. The final sizing for the dynamic components of the DC-DC converter used in the experimental validations is shown in Table 2. It should be noted that the ESR_{CIN} and ESR_C were reported in the table, but for simplicity, they were neglected in the circuit model.

Table 2. Dynamic component values.

Component	Measured
Inductance L	224.62 µH/ESR_L = 0.023 Ω
Capacitance C	662.32 µF/ESR_C = 0.016 Ω
Input Capacitance C_{IN}	2937.2µF/ESR_{CIN} = 0.016 Ω

4. Experimental Validation

The converter described in Section 3 was utilized in three different experimental workbenches (WB): WB1 involved the measurement of the dynamic response for the DC-DC converter at a constant voltage input. WB2 involved the steady-state response of the DC-DC converter with a real PV panel as an input and operated under outdoor variable environmental conditions. WB3 involved the dynamic response for the DC-DC converter with a hardware-simulated PV device as the input and a programmable load as an output. The experimental measurements of each WB are compared against the simulation based on the model described in Section 2.

4.1. WB1: Constant Voltage Input

The purpose of the first test is to assess the transient accuracy of the model for the DC-DC converter by itself, using as input a voltage source. As stated before, a PV source is drastically different from a voltage source, but we consider this first test important for the setup of the approach. By removing the main nonlinearity from the system (i.e., the PV device), this allows for an analysis that is focused only on the transient evolution of the fast-dynamic elements of the converter. The measurements and the simulations represent the turn-on transient of the DC-DC converter with a constant input voltage. The transient measurements were acquired using a dSPACE MicroLabBox (dSPACE Inc. Wixom, MI, USA), which is an integrated solution for measurement and hardware development. The system is based on an NXP (NXP Semiconductors Netherlands, Eindhoven) processor (dual core, 2 GHz), features eight analog input channels with independent ADC conversion (14-bit and 10 Msps) and a voltage range of ±10 V. The system features analog outputs as well, with 16 channels featuring independent DAC conversion (16-bit and 1 Msps). Moreover, the system features 48 digital I/O ports

configurable to implement the most common digital interfaces (e.g., CAN, I2C, SPI, etc.). For the purpose of this setup, the digital output of the dSPACE was used to create the driving signal for the Pulse Width Modulation (PWM) of the DC-DC converter, and the analog inputs were used to sample the input and output voltage of the converter. The results of the output voltage at constant input voltages of 5 V and 7 V are shown in Figure 4.

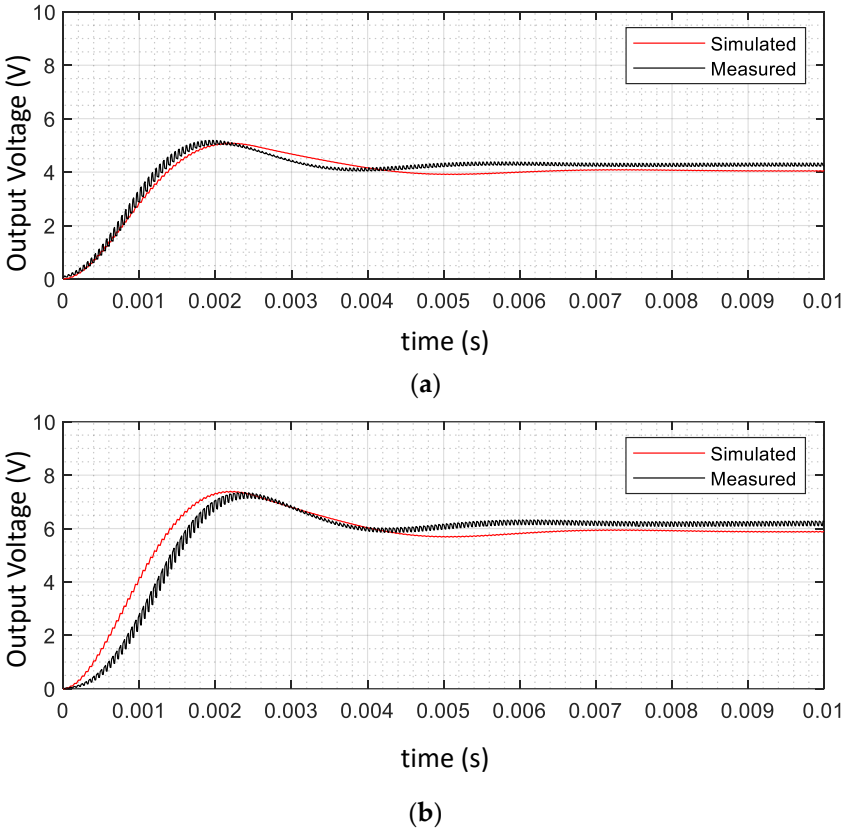

Figure 4. Turn-on transient response of the converter with constant input voltages: 5 V (**a**) and 7 V (**b**).

4.2. WB2: Outdoor PV

The purpose of the second test is to assess the steady-state accuracy of the model when a real PV panel is utilized as a source. The steady-state value is strongly influenced by the environmental values of irradiance and temperature. For this reason, an outdoor setup was implemented featuring a 230-W PV Panel TW230P60-FA2 by Tianwei, Changhua, Taiwan(a datasheet extract showing the open circuit voltage V_{OC}, the short circuit current I_{SC}, the maximum power voltage V_{MP} and the maximum power current I_{MP} can be seen in Table 3) and an instrumental chain for the acquisition of instantaneous irradiance, panel backside temperature, DC-DC input voltage, and DC-DC output voltage. The measurements are performed using a dedicated instrument for PV panel testing, the Chauvin Arnoux Green Test FTV100 by Chauvin Arnoux, Paris, France. This instrument features input ports for both AC and DC voltage and the current measurements, along with a set of input ports for the temperature and irradiance probes. For the purpose of this test, the DC ports for voltage (up to 1000 V) and current (up to 200 A) were used. The temperature was measured through a PT100 temperature probe by Chauvin Arnoux, Paris, France (−30 to 80 °C range with 1% accuracy), and the solar irradiance was measured through a pyranometer by Chauvin Arnoux, Paris, France (up to a 2000 W/m^2 range with 2% accuracy). For this measurement, a constant load resistance 11 Ω and three different duty cycles (40%, 50%, and 60%) were used; the choice was done to test the system in a mid-working condition. Measurements were performed in January 2020 at 43.799° N. The measurement chain is schematized in Figure 5, along with the electrical characteristics of the panel in Figure 6.

The field implementation is shown in Figure 7. The irradiance values and temperature (Figure 8) recorded by the FTV100 were used to simulate the PV device under variable conditions. The Chauvin Arnoux was configured to average the temperature and irradiance measurements over 10 s. Thus, 300 points is a measurement spanning over 50 min. The small irradiance values are a consequence of the local weather during the tests. It is worth noticing that obtaining a good steady-state accuracy at low irradiances is much more difficult than at quasi-SRC, due to the behavior of the R_{SH} parameter of the one-diode model for low values of G. The steady-state input and output voltages, simulated and measured, are shown in Figure 9.

Table 3. TW230P60 electrical characteristics.

V_{OC} (V)	I_{SC} (A)	V_{MP} (V)	I_{MP} (A)
37.3	8.22	29.4	7.82

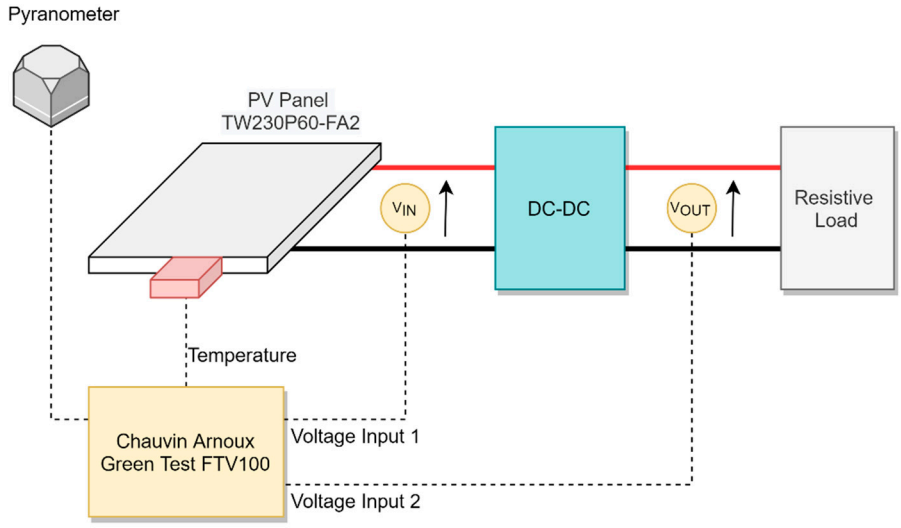

Figure 5. Measurement chain for the steady-state response over a variable irradiance and temperature.

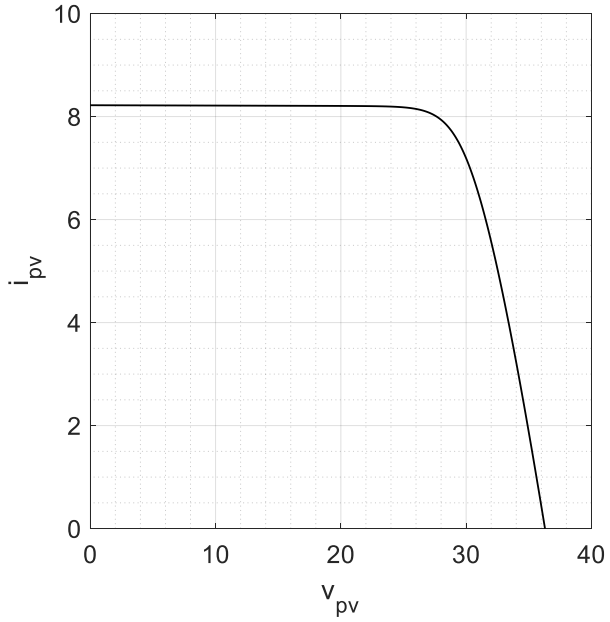

Figure 6. Electrical characteristics of the TW230P60-FA2 panel at the standard reference conditions (SRC).

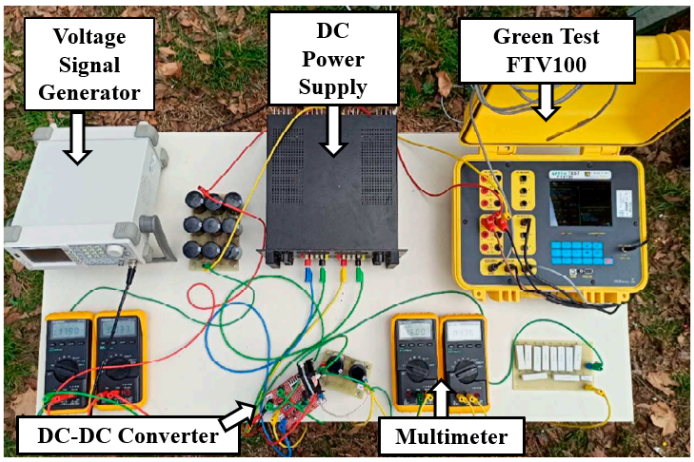

Figure 7. Experimental workbench for the outdoor PV test.

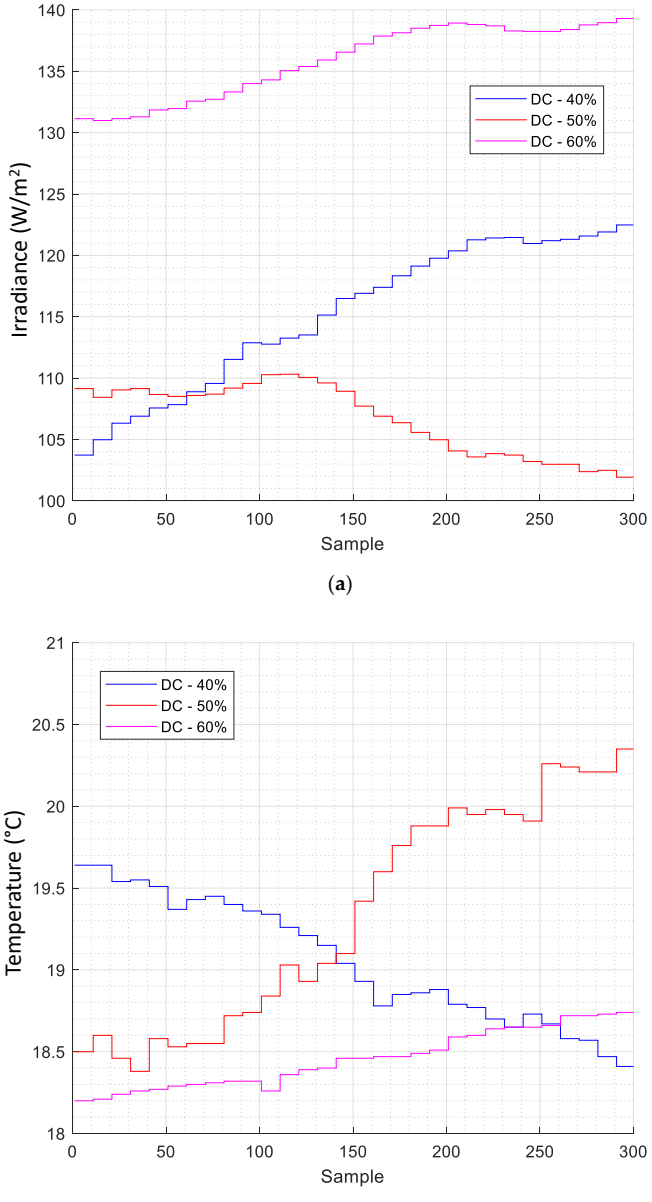

Figure 8. Irradiance (**a**) and temperature (**b**) conditions recorded during the measurement.

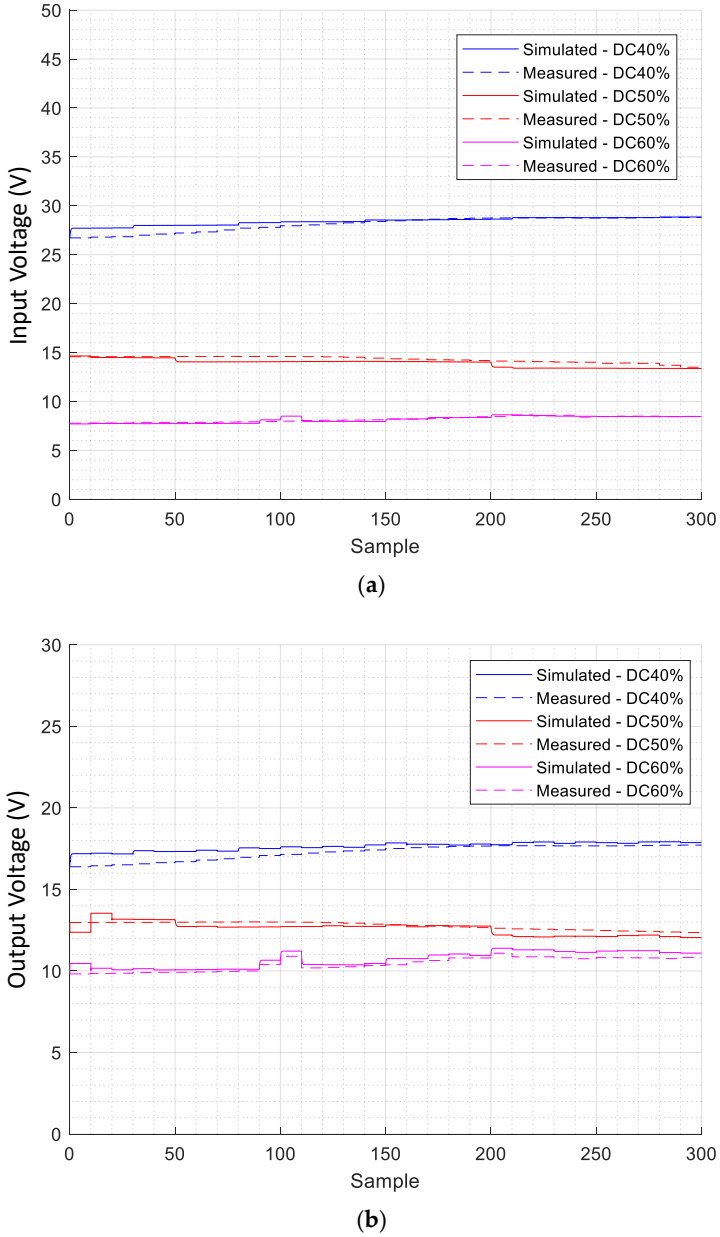

Figure 9. Simulated and measured steady-state input (**a**) and output (**b**) voltages.

4.3. WB3: Variable Output Load

The purpose of the third test is to assess the transient accuracy of the model when a PV source is present. Since changes in the irradiance and temperature are, in general, very slow if compared to the time constants of the system, there is no real interest in simulating the transient involved in them. On the other hand, the output load can change abruptly if a sudden energy sink is present. For the purpose of the experimental validation, this scenario was created by using a step-variable load. The measurement chain, schematized in Figure 10 and shown in Figure 11, is composed by a four-channel oscilloscope (Tektronix TDS3014b by Tektronix, Inc. Beaverton, OR, USA), a 700-W PV Device programmable simulator (TerraSAS ETS60), and a programmable AC-DC load (Itech IT 8615). A summary of the instrument's relevant characteristics is shown in Table 4. In particular, the PV simulator was programmed to simulate the panel reported in Table 5. The programmable load was programmed to switch between the values of 7.5 Ω and 17.5 Ω. The choice for these values was made considering that the PV device would work at the SRC, and for this I-V relationship, the panel would

switch from a quasi-SC (Short Circuit) condition (at 7.5 Ω) to a quasi-OC (Open Circuit) condition (at 17.5 Ω), achieving a large transient. The duty cycle of the DC-DC converter was kept at $D = 0.5$. The results of the two tests are shown in Figures 12 and 13. In the first one, the load resistance initially is 17.5 Ω and is commuted to 7.5 Ω once a steady state is reached. In the second one, the initial load resistance is 7.5 Ω and is commuted to 17.5 Ω before the steady state is reached. All the performed experimental tests confirm that the model correctly simulates both the transient and steady-state operations of the considered systems.

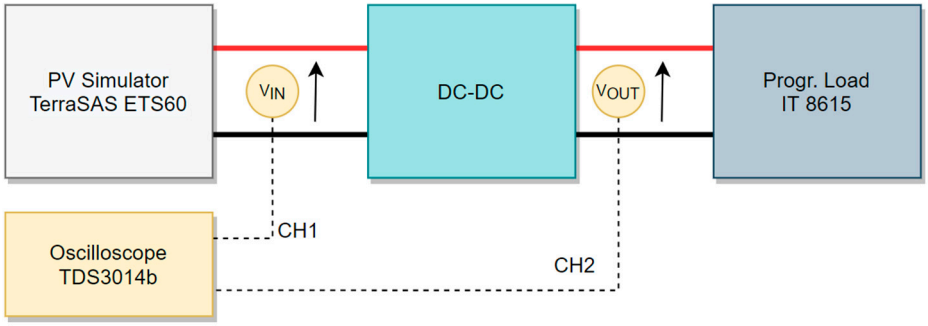

Figure 10. Measurement chain for the transient response over a step-variable load change.

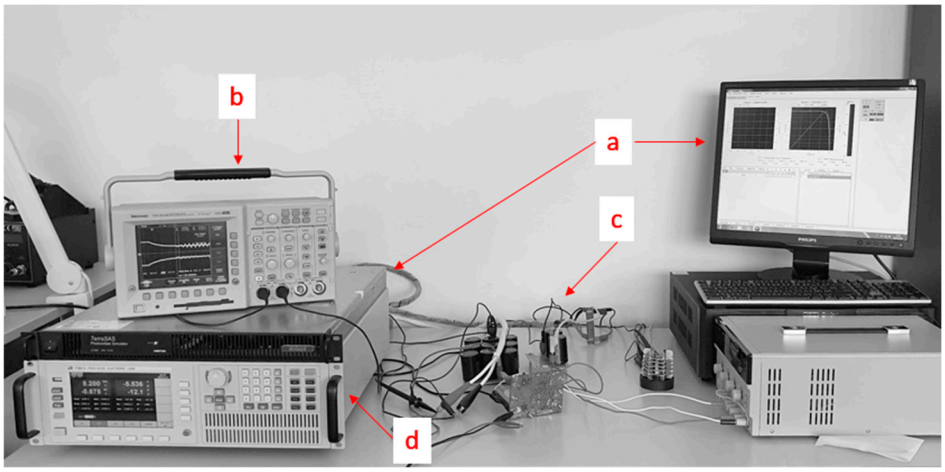

Figure 11. Experimental workbench depicting the TerraSAS ETS60 (**a**), the TDS3014b (**b**), the DC-DC converter (**c**), and the IT8615 (**d**).

Table 4. Instrumental chain of the workbench 3 (WB3) summary.

Instrument	Characteristics
Tektronix TDS3014b Oscilloscope	Four channels, up to 100 MHz 1 mV/div to 10 V/div vert. sensitivity 4 ns/div minimal time base GPIB and LAN connectivity
Itech IT 8615 Electronic Load	Up to 420 Vrms range and 1800 VA 45-Hz to 450-Hz frequency range GPIB, LAN, and USB connectivity
TerraSAS ETS60 Solar Simulator	Output up to 66 V (OC) and 14 A (SC) Maximum output power 714 W I-V curve resolution of 1024 points LAN connectivity

Table 5. Parameters for the PV simulator.

V_{OC} (V)	I_{SC} (A)	V_{MP} (V)	I_{MP} (A)
20	1.10	17.22	1.04

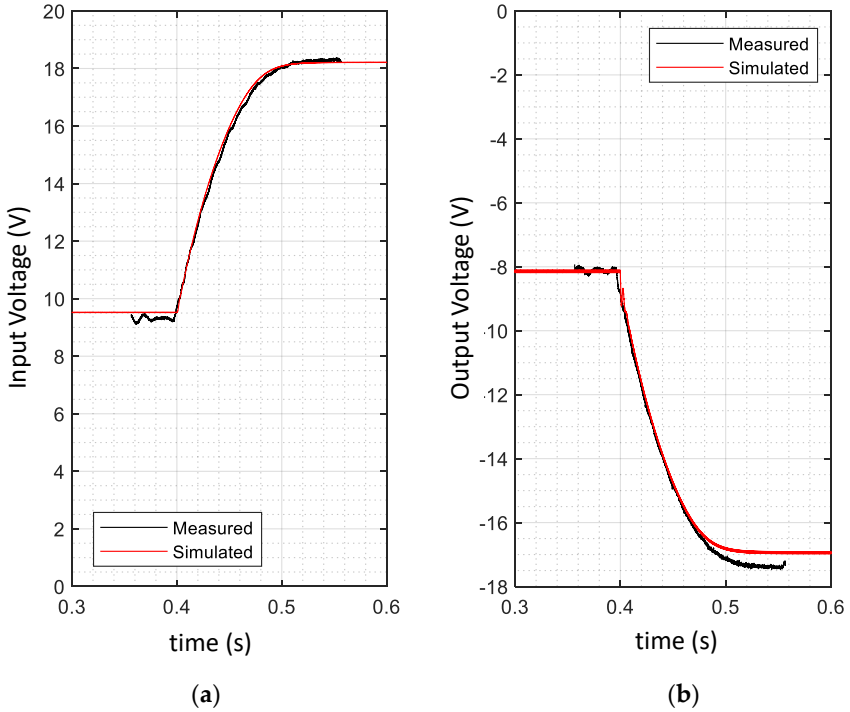

(**a**) (**b**)

Figure 12. Transient evolution of the input voltage (**a**) and output voltage (**b**) for an output load change from 7.5 Ω to 17.5 Ω.

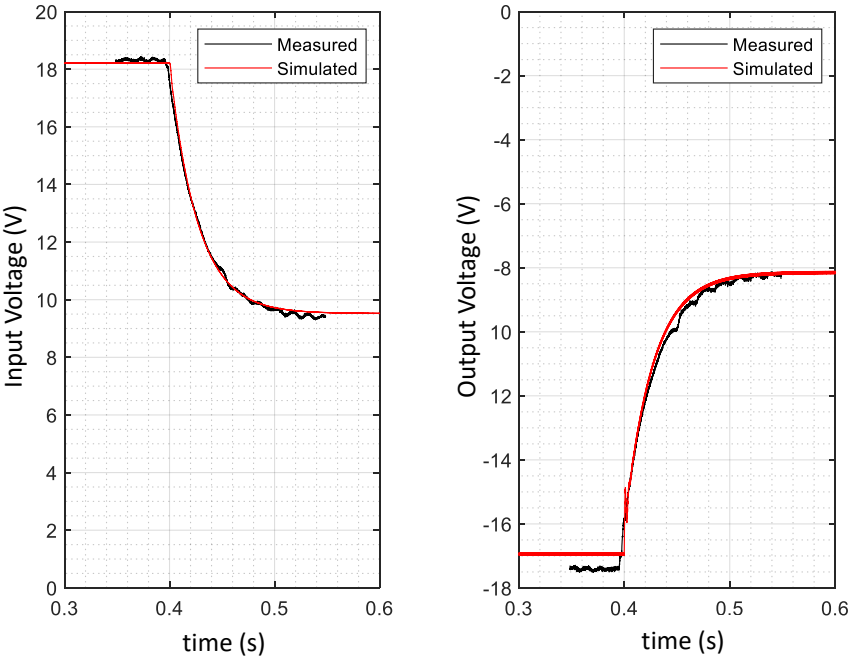

(a) (b)

Figure 13. Transient evolution of the input voltage (**a**) and output voltage (**b**) for an output load change from 17.5 Ω to 7.5 Ω.

The results obtained from this last workbench confirm the accuracy of the dynamic model even in presence of the PV device nonlinearity. Although a small error can be seen in the steady-state parts (which can be accounted for considering the nonideal connections), the transient evolution timings match almost perfectly the simulation. This is particularly meaningful if this model is to be used for the study of the DC-DC converter control systems, such as an MPPT controller, where an incorrect estimate of the time required for the system response could result in a completely different behavior between the simulations and the real system.

5. Conclusions

In this paper, an efficient and accurate methodology to simulate a DC-DC converter in photovoltaic applications was proposed, with the aim of creating a framework suitable for further integration in larger simulation and analysis environments. The proposed model was formulated to represent both the physical-to-electrical behavior of a photovoltaic device (i.e., taking into account nonelectrical quantities such as temperature and irradiance) and the dynamic nature of the DC-DC converter. The accuracy of the proposed approach was validated against three different experimental workbenches (two for the transient response and one for the steady-state response) to assess the reliability of the approach. The model in the steady state can be integrated with state-of-the-art measurements and the forecasting of irradiance [17–19] for power plant-produced energy estimations, and, in general, to assess the electrical quantities of the system over a large timespan. The dynamic model is crucial for innovative photovoltaic applications, such as automotive [41], where sudden changes in the environmental quantities often perturb the steady state, or PV systems, with highly variable power absorptions.

The possibility of integration for such a model in larger structures, which is the main aim of this research, is related to its computational efficiency and the wide adaptability that comes from its constituent parts. The single-diode model might not be the most accurate model for PV devices in the literature (more accurate, yet slower, is the double-diode model [42]), but it is a standard de facto for the representation of silicon devices, has solid literature concerning the model identification, and is computationally light. Moreover, the state-space approach, and the explicit current-voltage characteristics introduced for the PV device, make the methodology described in this work applicable to many different DC-DC converter topologies.

The methodology has, indeed, possible evolution and open problems. The choice of the single-diode model was widely justified for silicon devices, yet for some new technologies such as organic PV, it would be interesting to implement and validate other, more complex, circuit models [43,44]. To make this inclusion viable from a computational point of view, it might require numerical optimization of the circuit relations describing the models [45,46].

A second interesting possibility is to further extend the model chain. On the PV side, the model could be coupled with forecasting or measurement methodologies for the environmental quantities of irradiance and temperature [17–19]. On the load side, grid connection could be considered along with a load profile. This later quantity, analogously to the environmental quantities of irradiance and temperature, has a large literature field concerning measurement and forecasting [47–49].

Author Contributions: Conceptualization and supervision, A.L. and A.R.; methodology, A.L. and G.M.L.; investigation, G.M.L. and F.C.; validation, G.M.L. and A.L.; and prototyping and measurements, A.R. and F.C., manuscript writing F.C. and G.M.L., manuscript revision A.L. and A.R. All authors have read and agreed to the published version of the manuscript.

Funding: This research received no external funding.

Conflicts of Interest: The authors declare no conflict of interest.

References

1. Nousiainen, L.; Puukko, J.; Mäki, A.; Messo, T.; Huusari, J.; Jokipii, J.; Viinamäki, J.; Lobera, D.T.; Valkealahti, S.; Suntio, T. Photovoltaic generator as an input source for power electronic converters. *IEEE Trans. Power Electron.* **2013**, *28*, 3028–3038. [CrossRef]
2. Agorreta, J.L.; Borrega, M.; López, J.; Marroyo, L. Modeling and control of N-paralleled grid-connected inverters with LCL filter coupled due to grid impedance in PV plants. *IEEE Trans. Power Electron.* **2011**, *26*, 770–785. [CrossRef]
3. Figueres, E.; Garcerá, G.; Sandia, J.; González-Espín, F.; Rubio, J.C. Sensitivity study of the dynamics of three-phase photovoltaic inverters with an LCL grid filter. *Proc. IEEE Trans. Ind. Electron.* **2009**, *56*, 706–717. [CrossRef]
4. Suntio, T.; Leppäaho, J.; Huusari, J.; Nousiainen, L. Issues on solar-generator interfacing with current-fed MPP-tracking converters. *IEEE Trans. Power Electron.* **2010**, *25*, 2409–2419. [CrossRef]
5. Luchetta, A.; Manetti, S.; Piccirilli, M.C.; Reatti, A.; Kazimierczuk, M.K. Comparison of DCM operated PWM DC-DC converter modelling methods including the effects of parasitic components on duty ratio constraint. In Proceedings of the 2015 IEEE 15th International Conference on Environment and Electrical Engineering, Rome, Italy, 10–13 June 2015.
6. Davoudi, A.; Jatskevich, J.; Chapman, P.L. Averaged modelling of switched-inductor cells considering conduction losses in discontinuous mode. *IET Electr. Power Appl.* **2007**, *1*, 402–406. [CrossRef]
7. Luchetta, A.; Manetti, S.; Piccirilli, M.C.; Reatti, A.; Kazimierczuk, M.K. Effects of parasitic components on diode duty cycle and small-signal model of PWM DC-DC buck converter in DCM. In Proceedings of the 2015 IEEE 15th International Conference on Environment and Electrical Engineering, Rome, Italy, 10–13 June 2015.
8. Kazimierczuk, M.K. *Pulse-Width Modulated DC-DC Power Converters*, 2nd ed.; John Wiley & Sons, Inc.: New York, NY, USA, 2015; ISBN 9781119009524.
9. Davoudi, A.; Jatskevich, J.; Chapman, P.L. Simple method of including conduction losses for average modelling of switched-inductor cells. *Electron. Lett.* **2006**, *42*, 1246–1248. [CrossRef]
10. Amir, S.; Van Der Zee, R.; Nauta, B. An improved modeling and analysis technique for peak current-mode control-based boost converters. *IEEE Trans. Power Electron.* **2015**, *30*, 5309–5317. [CrossRef]
11. Davoudi, A.; Jatskevich, J.; Chapman, P.L. Numerical dynamic characterization of peak current-mode-controlled DC-DC converters. *IEEE Trans. Circuits Syst. II Express Briefs* **2009**, *56*, 906–910. [CrossRef]
12. Reatti, A.; Balzani, M. Computer aided small-signal analysis for PWM DC-DC converters operated in discontinuous conduction mode. In Proceedings of the Midwest Symposium on Circuits and Systems, Covington, KY, USA, 7–10 August 2005.
13. Ayachit, A.; Reatti, A.; Kazimierczuk, M.K. Small-signal modeling of PWM dual-SEPIC DC-DC converter by circuit averaging technique. In Proceedings of the IECON Proceedings (Industrial Electronics Conference), Florence, Italy, 23–26 October 2016.
14. Díaz-González, F.; Sumper, A.; Gomis-Bellmunt, O.; Villafáfila-Robles, R. A review of energy storage technologies for wind power applications. *Renew. Sustain. Energy Rev.* **2012**, *16*, 2154–2171. [CrossRef]
15. González, A.; Goikolea, E.; Barrena, J.A.; Mysyk, R. Review on supercapacitors: Technologies and materials. *Renew. Sustain. Energy Rev.* **2016**, *58*, 1189–1206. [CrossRef]
16. Lorenz, E.; Hurka, J.; Heinemann, D.; Beyer, H.G. Irradiance Forecasting for the Power Prediction of Grid-Connected Photovoltaic Systems. *IEEE J. Sel. Top. Appl. Earth Obs. Remote Sens.* **2009**, *2*, 2–10. [CrossRef]
17. Diagne, M.; David, M.; Lauret, P.; Boland, J.; Schmutz, N. Review of solar irradiance forecasting methods and a proposition for small-scale insular grids. *Renew. Sustain. Energy Rev.* **2013**, *27*, 65–76. [CrossRef]
18. Dong, Z.; Yang, D.; Reindl, T.; Walsh, W.M. Short-term solar irradiance forecasting using exponential smoothing state space model. *Energy* **2013**, *55*, 1104–1113. [CrossRef]
19. Oliveri, A.; Cassottana, L.; Laudani, A.; Riganti Fulginei, F.; Lozito, G.M.; Salvini, A.; Storace, M. Two FPGA-Oriented High-Speed Irradiance Virtual Sensors for Photovoltaic Plants. *IEEE Trans. Ind. Inform.* **2017**, *13*, 157–165. [CrossRef]
20. Suntio, T.; Messo, T.; Aapro, A.; Kivimäki, J.; Kuperman, A. Review of PV generator as an input source for power electronic converters. *Energies* **2017**, *10*, 1076. [CrossRef]

21. Catelani, M.; Ciani, L.; Kazimierczuk, M.K.; Reatti, A. Matlab PV solar concentrator performance prediction based on triple junction solar cell model. *Meas. J. Int. Meas. Confed.* **2016**, *88*, 310–317. [CrossRef]
22. Laudani, A.; Riganti Fulginei, F.; Salvini, A. Identification of the one-diode model for photovoltaic modules from datasheet values. *Sol. Energy* **2014**, *108*, 432–446. [CrossRef]
23. De Soto, W.; Klein, S.A.; Beckman, W.A. Improvement and validation of a model for photovoltaic array performance. *Sol. Energy* **2006**, *80*, 78–88. [CrossRef]
24. Corless, R.M.; Gonnet, G.H.; Hare, D.E.G.; Jeffrey, D.J.; Knuth, D.E. On the Lambert W function. *Adv. Comput. Math.* **1996**, *5*, 329–359. [CrossRef]
25. Blakesley, J.C.; Castro, F.A.; Koutsourakis, G.; Laudani, A.; Lozito, G.M.; Riganti Fulginei, F. Towards non-destructive individual cell I-V characteristic curve extraction from photovoltaic module measurements. *Sol. Energy* **2020**, *202*, 342–357. [CrossRef]
26. Roberts, K.; Valluri, S.R. Solar Cells and the Lambert W Function. In *Celebrating 20 Years of the Lambert W Function*; London, ON, Canada, 2016.
27. Abdulkadir, M.; Samosir, A.S.; Yatim, A.H.M. Modelling and simulation of maximum power point tracking of photovoltaic system in Simulink model. In Proceedings of the 2012 IEEE International Conference on Power and Energy (PECon), Kota Kinabalu, Malaysia, 2–5 December 2012; pp. 325–330.
28. Suskis, P.; Galkin, I. Enhanced photovoltaic panel model for MATLAB-simulink environment considering solar cell junction capacitance. In Proceedings of the IECON 2013-39th Annual Conference of the IEEE Industrial Electronics Society, Vienna, Austria, 10–13 November 2013; pp. 1613–1618.
29. Kharb, R.K.; Shimi, S.L.; Chatterji, S.; Ansari, M.F. Modeling of solar PV module and maximum power point tracking using ANFIS. *Renew. Sustain. Energy Rev.* **2014**, *33*, 602–612. [CrossRef]
30. Takruri, M.; Farhat, M.; Barambones, O.; Ramos-Hernanz, J.A.; Turkieh, M.J.; Badawi, M.; AlZoubi, H.; Abdus Sakur, M. Maximum Power Point Tracking of PV System Based on Machine Learning. *Energies* **2020**, *13*, 692. [CrossRef]
31. Du, Y.; Yan, K.; Ren, Z.; Xiao, W. Designing localized MPPT for PV systems using fuzzy-weighted extreme learning machine. *Energies* **2018**, *11*, 2615. [CrossRef]
32. Ahmad, S.; Hasan, N.; Bharath Kurukuru, V.S.; Ali Khan, M.; Haque, A. Fault Classification for Single Phase Photovoltaic Systems using Machine Learning Techniques. In Proceedings of the 2018 8th IEEE India International Conference on Power Electronics (IICPE), Jaipur, India, 13–15 December 2018; pp. 1–6.
33. Laudani, A.; Riganti Fulginei, F.; Salvini, A. High performing extraction procedure for the one-diode model of a photovoltaic panel from experimental I-V curves by using reduced forms. *Sol. Energy* **2014**, *103*, 316–326. [CrossRef]
34. Shiau, J.K.; Ma, C.W. Li-Ion battery charging with a buck-boost power converter for a solar powered battery management system. *Energies* **2013**, *6*, 1669–1699. [CrossRef]
35. Tang, M.; Stuart, T. Selective buck-boost equalizer for series battery packs. *IEEE Trans. Aerosp. Electron. Syst.* **2000**, *36*, 201–211. [CrossRef]
36. Arsalan, M.; Iftikhar, R.; Ahmad, I.; Hasan, A.; Sabahat, K.; Javeria, A. MPPT for photovoltaic system using nonlinear backstepping controller with integral action. *Sol. Energy* **2018**, *170*, 192–200. [CrossRef]
37. Davoudi, A.; Jatskevich, J.; De Rybel, T. Numerical state-space average-value modeling of PWM dc-dc converters operating in DCM and CCM. *IEEE Trans. Power Electron.* **2006**, *21*, 1003–1012. [CrossRef]
38. Pavlovic, T.; Bjazi, T.; Ban, Ž. Simplified averaged models of dc-dc power converters suitable for controller design and microgrid simulation. *IEEE Trans. Power Electron.* **2013**, *28*, 3266–3275. [CrossRef]
39. Babaei, E.; Seyed Mahmoodieh, M.E.; Mashinchi Mahery, H. Operational modes and output-voltage-ripple analysis and design considerations of buck-boost DC-DC converters. *IEEE Trans. Ind. Electron.* **2012**, *59*, 381–391. [CrossRef]
40. Texas Instruments SLVA721A—Basic Calculation of an Inverting Buck-Boost Power Stage. 2017. Available online: https://www.ti.com/lit/an/slva721a/slva721a.pdf (accessed on 29 September 2020).
41. Cheddadi, Y.; Errahimi, F.; Es-sbai, N. Design and verification of photovoltaic MPPT algorithm as an automotive-based embedded software. *Sol. Energy* **2018**, *171*, 414–425. [CrossRef]
42. Humada, A.M.; Hojabri, M.; Mekhilef, S.; Hamada, H.M. Solar cell parameters extraction based on single and double-diode models: A review. *Renew. Sustain. Energy Rev.* **2016**, *56*, 494–509. [CrossRef]
43. Mazhari, B. An improved solar cell circuit model for organic solar cells. *Sol. Energy Mater. Sol. Cells* **2006**, *90*, 1021–1033. [CrossRef]

44. Cheknane, A.; Hilal, H.S.; Djeffal, F.; Benyoucef, B.; Charles, J.-P. An equivalent circuit approach to organic solar cell modelling. *Microelectron. J.* **2008**, *39*, 1173–1180. [CrossRef]
45. Lun, S.; Wang, S.; Yang, G.H.; Guo, T.T. A new explicit double-diode modeling method based on Lambert W-function for photovoltaic arrays. *Sol. Energy* **2015**, *116*, 69–82. [CrossRef]
46. Gao, X.; Cui, Y.; Hu, J.; Xu, G.; Yu, Y. Lambert W-function based exact representation for double diode model of solar cells: Comparison on fitness and parameter extraction. *Energy Convers. Manag.* **2016**, *127*, 443–460. [CrossRef]
47. Wen, L.; Zhou, K.; Yang, S.; Lu, X. Optimal load dispatch of community microgrid with deep learning based solar power and load forecasting. *Energy* **2019**, *171*, 1053–1065. [CrossRef]
48. Li, L.; Ota, K.; Dong, M. When weather matters: IoT-based electrical load forecasting for smart grid. *IEEE Commun. Mag.* **2017**, *55*, 46–51. [CrossRef]
49. Raza, M.Q.; Khosravi, A. A review on artificial intelligence based load demand forecasting techniques for smart grid and buildings. *Renew. Sustain. Energy Rev.* **2015**, *50*, 1352–1372. [CrossRef]